ACS OMEGA

http://pubs.acs.org/journal/acsodf

Article

Theoretical Study on Photothermal Properties of Azobenzene Sulfonate/Magnesium−Aluminum Hydroxide Composite Dye

Peihuan Zhang, Yue Zhu, Zhewei Li, Luocong Wang, Caiwei Yue, Ming Lei,* and Min Pu*

Cite This: *ACS Omega* 2023, 8, 11596−11606

Read Online

ACCESS | Metrics & More | Article Recommendations | Supporting Information

ABSTRACT: The assembly of various azo dyes and pigments with inorganic layered materials could develop new types of intercalation materials. The electronic structures and photothermal properties of composite materials (AbS^--LDH) constituted by azobenzene sulfonate anions (AbS^-) and Mg−Al layered double hydroxide (LDH) lamella were theoretically studied at the M06-2X/def2-TZVP//M06-2X/6-31G(d,p) level using density functional theory and time-dependent density functional theory. Meanwhile, the influences of LDH lamella on the AbS^- in AbS^--LDH materials were investigated. The calculated results showed that the addition of LDH lamella could lower the isomerization energy barrier of $CAbS^-$ anions ($CAbS^-$ stands for *cis* AbS^-). The thermal isomerization mechanisms of AbS^--LDH and AbS were related to the conformational change of the azo group, out-of-plane rotation and in-plane inversion. The LDH lamella could reduce the energy gap of the n → π* and π → π* electronic transition and lead to a red-shift in the absorption spectra. When a polar solvent DMSO was applied, the excitation energy of the AbS^--LDHs was increased, making its photostability stronger than in nonpolar solvent and solvent-free.

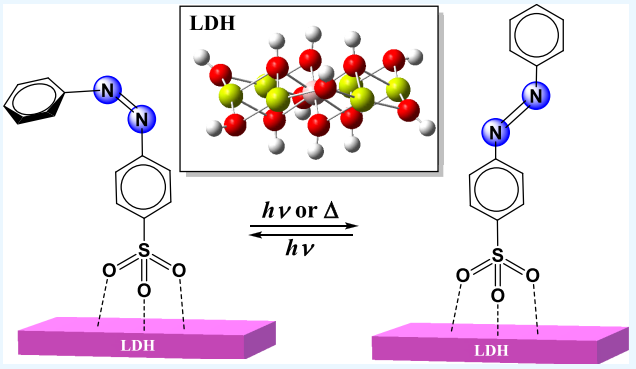

1. INTRODUCTION

Azobenzene dyes are a class of functional materials that can be modified by thermal and photochemical treatment, which could have wide applications in molecular switches, molecular machines, memory storage, and nanodevices.[1−12] As known to all, azobenzene dye could undergo a reversible isomerization between *cis* and *trans* conformations at appropriate conditions. There are two possible isomerization pathways: via rotation or inversion. The former proceeds via an out-of-plane rotation of a benzene ring around the N═N double bond, and the latter proceeds via an in-plane inversion by increasing the NNC angle to 180°. A thermally induced *cis* to *trans* isomerization of azobenzene readily occurs in the ground state.[13−17] The *cis* structure of azobenzene dyes may be converted to the *trans* one at room temperature and could be accelerated by visible light irradiation, so their relatively poor thermal stability limit azobenzene dyes' practical application. It is very meaningful to assemble azobenzene dyes into different carrier materials to increase their stabilities and unveil the nature of the isomerization mechanism. Takei et al. encapsulated methyl orange (MO) in a cyclodextrin cavity to study its isomerization and found that the isomerization can be hindered due to a strong intermolecular interaction induced by nanospace confinement.[18] Kojima et al. showed that the electrostatic interaction between azobenzene and the metal ions in the zeolite nanocavity could modulate the *cis*−*trans* isomerization process.[19] Therefore, it is of great significance to find new carrier materials to achieve stable host−guest composite materials capable of isomerization of azobenzene dyes.

As an important class of host−guest materials, layered double hydroxides (LDHs) is one of the promising host carrier candidates, which could provide a good microenvironment for the distribution of azobenzene guest molecules. LDH is a kind of inorganic material with characteristics of interlayer anion exchangeability, thermal stability, and tunability of the composition and structure of the lamellas.[20] Its special structure owns advantages of both a guest and host, which could be used in many fields such as catalysis, medicine, photochemistry, etc.[21−25] LDH lamellas are positively charged, and the interlayer anions could be replaced by other anions, so they can be used to prepare nanoscale organic/inorganic layered composites.[26] LDH films had been widely studied as components of optical, electrical, and magnetic devices, which made their preparations a rapidly growing research area in recent years.[27−29] One of the fascinating features of these LDH composite materials is that the intercalated ions could adopt

Received: February 7, 2023
Accepted: March 3, 2023
Published: March 14, 2023

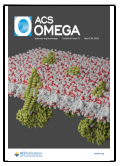

different arrangements and orientations in the interlayer space of LDH. The inorganic LDH host materials could effectively improve not only the optical stability but also the thermal stability of the intercalated organic dye. To improve the thermal stability of azo compounds and prepare the materials with new functions, a variety of azo dyes and pigments such as Naphthol Yellow S, Acid Orange II, Direct Yellow 50, etc. as guest molecules have been successfully intercalated into LDHs.[30−37] These research studies showed that the performances of composite intercalated materials were better than that of a single dye molecule and that many kinds of modified or novel intercalated materials could be used to prepare molecular devices. Svoboda et al. pointed out that the dye with a $-SO_3^-$ substituent intercalated into Zn-Al-LDH could be vertically arranged between layers and that the existence of inorganic layers might improve their thermal and optical stabilities.[32] However, the relationship between the physicochemical properties and structures of these host−guest LDH materials is still not clear.

Herein, we used an azobenzene sulfonate (AbS^-) anion as a guest molecule and Mg-Al-LDH lamella as a host. The combination of AbS^- anions with LDH lamella could form a new type of dye material. The isomerization pathways of 4,4-azobenzene disulfonate dye have been theoretically studied in our previous work,[38] which produced two sulfonic groups as electron-withdrawing substituents in the para-positions of azobenzene. Adopting an appropriate cluster model, the structures and properties of the composite materials could be investigated using high-level theoretical methods. This study focuses on the use of cluster models to explore the photo- and thermal properties of the composite (AbS^--LDH) constituted by azobenzene sulfonate anions (AbS^-) and Mg−Al hydroxide (LDH) lamella. Our previous studies on LDHs with a Mg/Al ratio of 2 or 3 have shown that their lowest unoccupied molecular orbitals (LUMO) could attract anions in the center of the lamella.[39,40] In this work, molecular structures, electronic spectra, and thermal *cis*−*trans* isomerization of azobenzene sulfonate anions with different substituent positions (*p*-azobenzene sulfonate: *p*-AbS; *m*-azobenzene sulfonate: *m*-AbS) combined with LDH lamella were studied by density functional theory (DFT) and time-dependent DFT (TD-DFT) calculations. In addition, the influence of LDH lamella on the AbS^- anion was also discussed by comparing the AbS's isomerization pathways of AbS^--LDH and the AbS molecule.

2. COMPUTATIONAL DETAILS

Using density functional theory (DFT), the thermal isomerization mechanisms of AbS^--LDH and the AbS single molecule were studied at the M06-2X/def2-TZVP//M06-2X/6-31G-(d,p) level.[41,42] The geometric optimization was carried out at the M06-2X/6-31G(d,p) level, and the single point energies and electronic property analysis were calculated at the M06-2X/def2-TZVP level. In addition, functional testing is presented in the Supporting Information. All structures of reactants, transition states, and products along reaction pathways were fully optimized, and the frequencies of all stationary points were calculated. The transition states were confirmed with one and only one imaginary frequency. The vertical excitation properties were also calculated using the TD-DFT method at the same level.[43,44] By comparing the UV spectra and difference in energy gaps of frontier orbitals of AbS^--LDH and AbS molecules, the influence of the Mg-Al-LDH lamella on the spectral properties of the AbS^- anion was discussed. The polar solvent DMSO and the non-polar solvent CCl_4 were used to calculate the solvent effect using the solvation model based on density (SMD). The Gaussian 09 program was used for all computations.[45]

3. RESULTS AND DISCUSSION

To study the influence of LDH lamella on azobenzene sulfonate dye, we carried out theoretical research with LDH1 and LDH2 as templates (see Figure 1, LDH1 and LDH2 refer

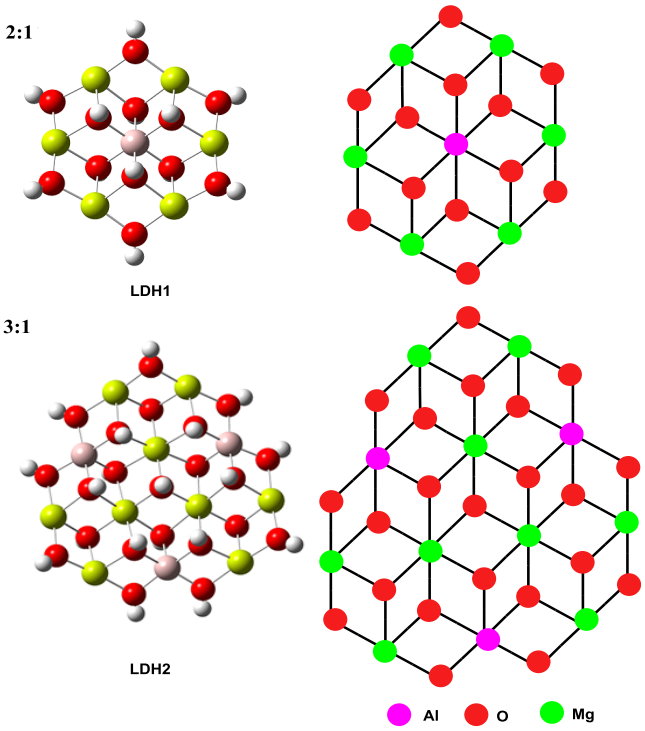

Figure 1. Optimized cluster models and corresponding chemdraw structures of LDH1 and LDH2 at the M06-2X/6-31G(d,p) level.

to LDH cluster models with Mg:Al = 2:1 and Mg:Al = 3:1, respectively). For the LDH1 structure, since Mg:Al = 2:1, the total charge is 2 and the spin multiplicity is 1. For the LDH2 structure, since Mg:Al = 3:1, the total charge is 4 and the spin multiplicity is 1.

3.1. Geometrical Structures. The structures of LDH lamella with different magnesium−aluminum ratios combined with AbS^- were optimized at the M06-2X/6-31G(d,p) level. As shown in Figure 2, $CAbS^-$ and $TAbS^-$ ($CAbS^-$ and $TAbS^-$ mean *cis* and *trans* azobenzene sulfonate) anions were arranged vertically on the lamella, and three O atoms of the $-SO_3^-$ group were connected to the H atoms of the hydroxyl groups of the Mg-Al-LDH lamella. When the Mg/Al ratio of LDH was 2:1, the distances between the O atoms of $-SO_3^-$ and H atoms of the hydroxyl group of the hydrotalcite lamella were 1.460−1.473 Å for *p*-$TAbS^-$-LDH1 and 1.459−1.487 Å for *m*-$TAbS^-$-LDH1, respectively, which implied that there were hydrogen bond interactions between $-SO_3^-$ and the lamella. When the Mg/Al ratio became 3:1, the distances between the O atoms of $-SO_3^-$ and H atoms of the hydroxyl group of the hydrotalcite lamella were 1.533−1.557 Å for *p*-$TAbS^-$-LDH2 and 1.539−1.571 Å for *m*-$TAbS^-$-LDH2, respectively. The distances between LDH1 and AbS^- were shorter than those of LDH2,

https://doi.org/10.1021/acsomega.3c00791
ACS Omega 2023, 8, 11596−11606

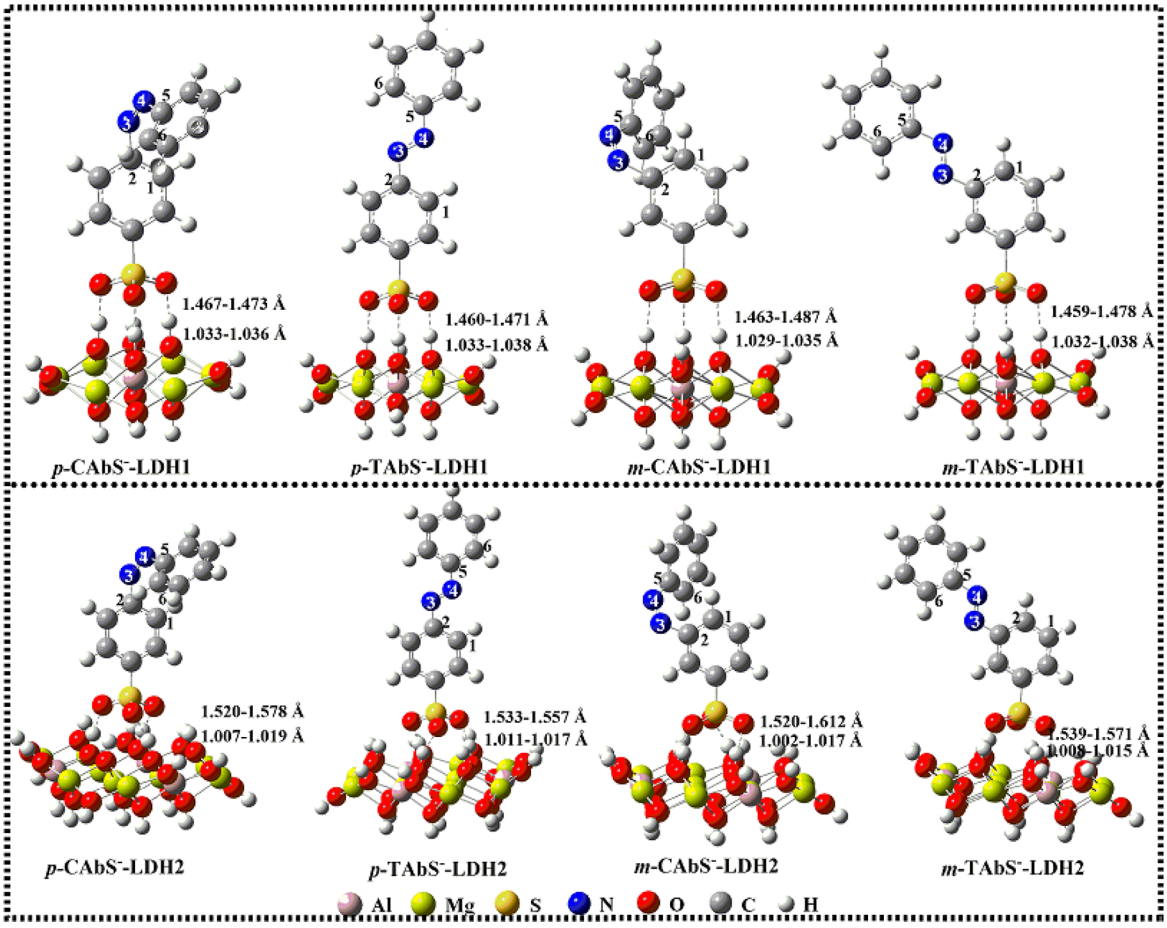

Figure 2. Optimized AbS⁻-LDHs' structures at the M06-2X/6-31G(d,p) level (-CAbS refers to *cis*-azobenzene sulfonic acid, -TAbS refers to *trans*-azobenzene sulfonic acid).

Table 1. Key Structural Parameters of Optimized AbS⁻-LDHs at the M06-2X/6-31G(d,p) Level.

	bond (Å)			dihedral angle (°)		
	C(2)-N(3)	N(3)-N(4)	N(4)-C(5)	∠C(1)C(2)N(3)N(4)	∠C(2)N(3)N(4)C(5)	∠C(6)C(5)N(4)N(3)
p-CAbS⁻-LDH1	1.431	1.237	1.434	−57.02	−8.88	−47.30
p-TAbS⁻-LDH1	1.425	1.248	1.415	3.62	−179.79	0.99
m-CAbS⁻-LDH1	1.438	1.238	1.434	50.86	7.91	49.65
m-TAbS⁻-LDH1	1.426	1.247	1.417	0.75	−179.85	0.46
p-CAbS⁻-LDH2	1.416	1.236	1.427	134.65	−11.68	−39.08
p-TAbS⁻-LDH2	1.415	1.255	1.402	2.30	−179.91	0.33
m-CAbS⁻-LDH2	1.437	1.239	1.428	47.02	9.13	45.93
m-TAbS⁻-LDH2	1.423	1.251	1.407	1.19	−179.81	0.56
p-CAbS	1.436	1.239	1.437	−55.11	−7.55	−50.57
p-TAbS	1.427	1.246	1.422	−0.29	−179.97	0.23
m-CAbS	1.438	1.39	1.438	54.24	7.57	51.89
m-TAbS	1.425	1.245	1.423	1.54	−179.88	0.60

indicating that the hydrogen bond interaction between AbS⁻ and LDH1 was stronger and the structure was more stable. The O−H bond lengths of the hydroxyl groups of LDH were increased from 0.965 to 1.033−1.038 Å (*p*-TAbS⁻-LDH1) and 1.011 to 1.017 Å (*p*-TAbS⁻-LDH2), respectively. It can be seen from Table 1 that the structural parameters of the main groups of AbS⁻ of AbS⁻-LDH and AbS single molecules were very close before and after assembly with LDH1 or LDH2. The dihedral angle ∠C(2)N(3)N(4)C(5) of *p*-TAbS⁻-LDH1 was −179.79°, which indicated that the two benzene rings were approximately in a plane. The dihedral angles of ∠C(1)C(2)-N(3)N(4) and ∠C(6)C(5)N(4)N(3) were 3.62 and 0.99°, respectively. Similarly, the two benzene rings of *m*-TAbS⁻-LDH1 were also approximately coplanar, and the dihedral angles of ∠C(2)N(3)N(4)C(5), ∠C(1)C(2)N(3)N(4), and ∠C(6)C(5)N(4)N(3) were −179.85, 0.75, and 0.46°, respectively. The relative energies (ΔG) are energy differences of *trans* structures of AbS⁻ anions, AbS molecules, and AbS⁻-LDH relative to *cis*. The $\Delta G_{p\text{-AbS}}$ and $\Delta G_{m\text{-TAbS}}$ were −12.7 and −13.4 kcal/mol, while the $\Delta G_{p\text{-AbS}^-\text{-LDH1}}$, $\Delta G_{m\text{-AbS}^-\text{-LDH1}}$, $\Delta G_{p\text{-AbS}^-\text{-LDH2}}$, and $\Delta G_{m\text{-AbS}^-\text{-LDH2}}$ were −15.6, −13.7, −19.3, and −18.2 kcal/mol as the AbS⁻ anion was assembled on the

https://doi.org/10.1021/acsomega.3c00791
ACS Omega 2023, 8, 11596−11606

LDH layer (see Figure 3). This indicated that the host Mg-Al-LDH lamella could improve the thermal stability of the intercalated AbS^- anions. The binding energy (E_B) of supramolecules were represented by the general formula: $E_B = E_{(AbS^-\text{-lamella})} - E_{(AbS^-)} - E_{(\text{lamella})}$. The calculated binding energies of *p*-$CAbS^-$-LDH1, *p*-$TAbS^-$-LDH1, *m*-$CAbS^-$-LDH1, and *m*-$TAbS^-$-LDH1 were −10.3, −10.4, −10.4, and −10.4 eV, respectively; those of *p*-$CAbS^-$-LDH2, *p*-$TAbS^-$-LDH2, *m*-$CAbS^-$-LDH2, and *m*-$TAbS^-$-LDH2 were −15.0, −15.3, −15.1, and −15.2 eV, respectively. This also demonstrated that host Mg-Al-LDH lamella could improve the thermal stability of the intercalated AbS^- anions.

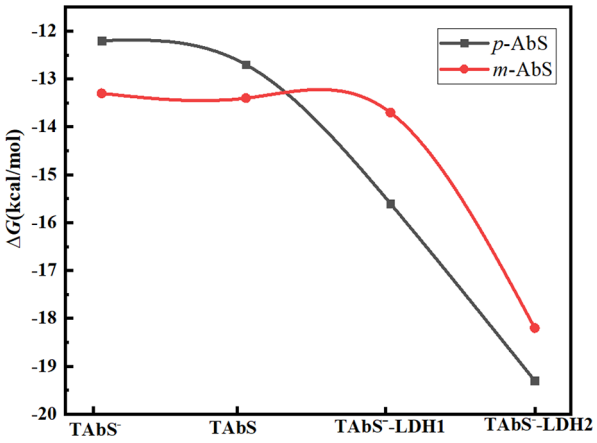

Figure 3. Free energies of *trans*-structures ($TAbS^-$, TAbS, $TAbS^-$-LDH1, and $TAbS^-$-LDH2) relative to their corresponding *cis*-structures ($CAbS^-$, CAbS, $CAbS^-$-LDH1, and $CAbS^-$-LDH2).

3.2. Thermal Isomerization of AbS Molecules with/without LDHs. The inversion and rotation isomerization pathways of AbS^--LDH and AbS molecules were discussed in the ground state in this study. The former can be achieved through the vibration of the N3 or N4 atom in the N═N double bond. The optimized geometric structures of stationary points along the isomerization pathways of AbS^--LDH1 are shown in Figure 4, and the key structural parameters are listed in Table 2. It could be seen from the geometric structures of transition states that two phenyl rings of *p*-AbS^- and *m*-AbS^- anions were neither perpendicular nor coplanar. The angle ∠N(2)N(3)C(4) of *p*-TS1-LDH1 was 178.91°, which was almost linear, and the dihedral angles ∠N(4)N(3)C(2)C(1) and N(3)N(4)C(5)C(6) were 76.75 and −0.47°, respectively. The angles ∠N(3)N(4)C(5) of *p*-TS2-LDH1 was 179.23°, which was almost linear, and the dihedral angles ∠N(4)N(3)-C(2)C(1) and N(3)N(4)C(5)C(6) were −4.76° and 26.07°, respectively. The dihedral angle ∠C(2)N(3)N(4)C(5) of *p*-

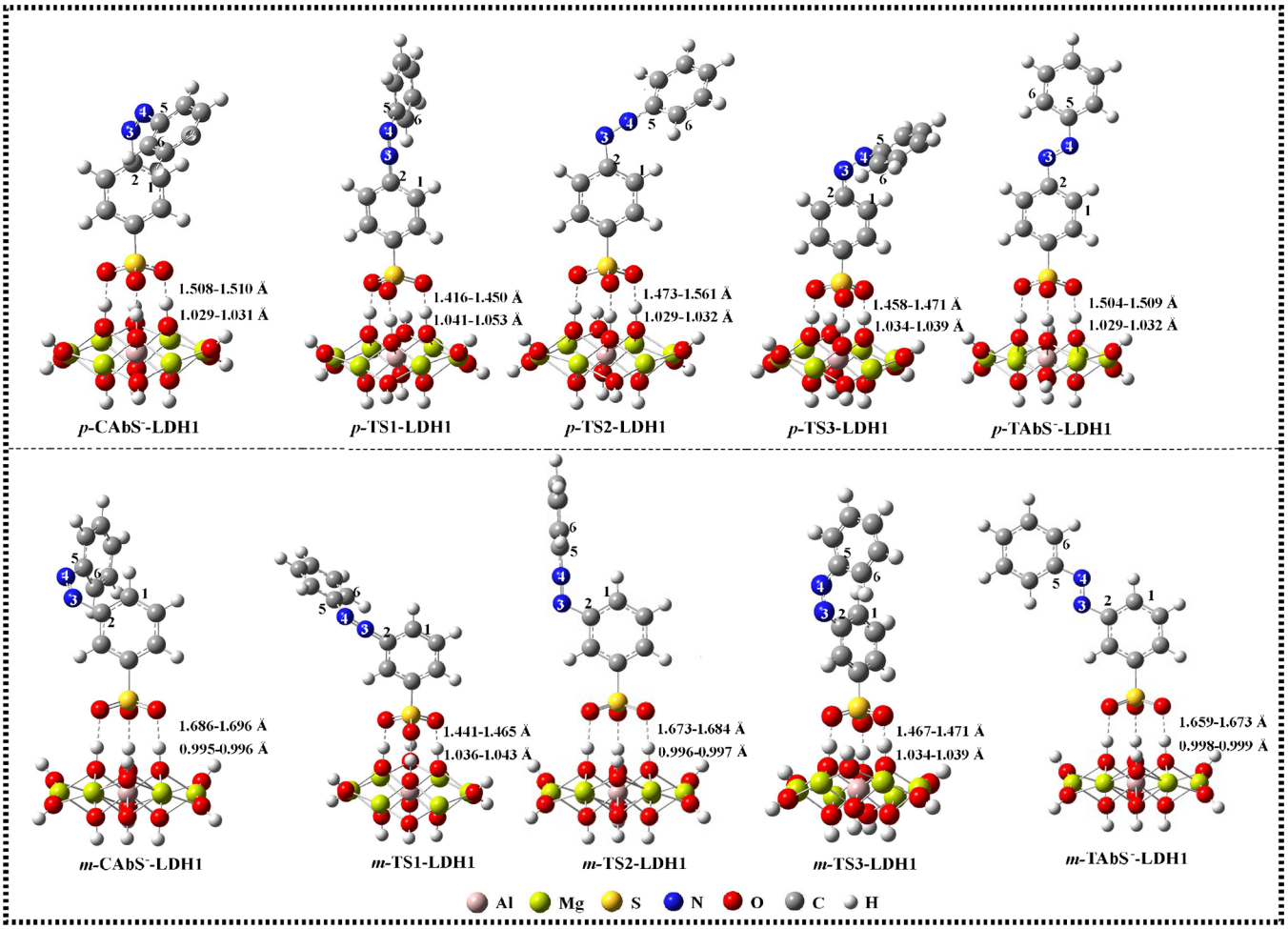

Figure 4. Optimized structures of stationary points along the isomerization pathways for *p*-$CAbS^-$-LDH1 and *m*-$CAbS^-$-LDH1 at the M06-2X/6-31G(d,p) level.

https://doi.org/10.1021/acsomega.3c00791
ACS Omega 2023, 8, 11596−11606

Table 2. Key Structural Parameters of Stationary Points along the Isomerization Pathways for *p*-CAbS$^-$-LDH1 and *m*-CAbS$^-$-LDH1 at the M06-2X/6-31G(d,p) Level.

	angle (°)			dihedral angle (°)	
	∠C(2) N(3) N(4)	∠N(3) N(4) C(5)	∠C(1) C(2) N(3) N(4)	∠C(2) N(3) N(4)C(5)	∠C(6) C(5) N(4) N(3)
p-CAbS$^-$-LDH1	125.94	124.10	−59.40	−11.36	−39.64
p-TS1-LDH1	178.91	117.75	76.75	13.41	−0.47
p-TS2-LDH1	116.31	179.23	−4.76	−80.43	26.07
p-TS3-LDH1	119.89	123.89	1.08	−88.87	0.73
p-TAbS$^-$-LDH1	113.65	115.66	1.19	179.82	−0.05
m-CAbS$^-$-LDH1	123.78	124.00	52.15	9.86	48.98
m-TS1-LDH1	120.40	117.17	0.84	86.47	−2.26
m-TS2-LDH1	116.81	179.22	−0.36	−123.77	31.88
m-TS3-LDH1	119.08	123.32	4.51	−88.26	1.40
m-TAbS$^-$-LDH1	114.54	114.70	0.82	−179.92	0.07

TS3-LDH1 was −88.87°, which was almost perpendicular. These angles and dihedral angles of the *m*-AbS$^-$ anion of *m*-TS-AbS$^-$-LDH1 were similar to those of the *p*-AbS$^-$ anion of *p*-TS-AbS$^-$-LDH1, which showed that the substituent positions of the phenyl rings of AbS$^-$ anions had little effect on the AbS$^-$ structure of AbS$^-$-LDH1. In the isomerization process of *p*-CAbS$^-$-LDH1, the angle ∠C(2)N(3)N(4) changed from 125.94 to 179.23° for *p*-TS1-LDH1 and then to 116.31° for *p*-TAbS$^-$-LDH1, and the angle ∠C(3)N(4)-N(5) changed from 124.10 to 179.23° for *p*-TS2-LDH1 and then to 115.66° for *p*-TAbS$^-$-LDH1, which both adopted an in-plane inversion pathway. The dihedral angle ∠C(2)N(3)-N(4)C(5) was from −11.36 to −88.87° for *p*-TS3-LDH1 and then to 179.82° for *p*-TAbS$^-$-LDH1, in which the unsubstituted benzene ring had an out-of-plane rotation. Similarly, the isomerization process of *m*-CAbS$^-$-LDH1 was close to the isomerization behaviors of *p*-CAbS$^-$-LDH1. The C(2)N(3)-N(4) and N(3)N(4)C(5) linear structures of transition states of isomerizations of *p*-AbS$^-$ and *m*-AbS$^-$ anions of *p*-TS-LDH1 and *m*-TS-LDH1 were due to the weakened coupling of the lone electron pairs of two N atoms, in which the hybrid orbital states of the N atoms changed from sp^2 to sp. Therefore, the isomerization processes of *p*-CAbS$^-$-LDH1 and *m*-CAbS$^-$-LDH1 were one-step concerted processes with the inversion of C(2)N(3)N(4) and the rotation of the unsubstituted benzene ring around the C(2)-N(3) bond. The isomerizations of AbS$^-$ in *p*-CAbS$^-$-LDH2 and *m*-CAbS$^-$-LDH2 were the same as those in *p*-CAbS$^-$-LDH1 and *m*-CAbS$^-$-LDH1 (see the optimized structures of stationary points along the isomerization pathways and key structural parameters for *p*-CAbS$^-$-LDH2 and *m*-CAbS$^-$-LDH2 in Figure S1 and Table S1 of the SI).

The free energy profiles of different isomerization pathways for *p*- and *m*-AbS$^-$-LDHs at the M06-2X/def2-TZVP//M06-2X/6-31G(d,p) level are shown in Figure 5. It can be seen that the inversion pathway through the N3 movement was more favorable than that through N4 movement and rotation in both para- and meta-positions for the AbS$^-$-LDHs. The energy barriers of the optimal thermal isomerization of *p*-AbS$^-$-LDH1, *m*-AbS$^-$-LDH1, *p*-AbS$^-$-LDH2, and *m*-AbS$^-$-LDH2 were 15.7, 22.0, 7.5, and 16.9 kcal/mol, respectively. It is obvious that the isomerization of *p*-CAbS-LDH2 is easier than others.

To explain the effect of lamellas on the isomerization of AbS$^-$ anions in AbS$^-$-LDH, the differences in the isomerization pathways between AbS and AbS$^-$-LDH were compared. The free energy profiles of isomerization pathways for *p*- and *m*-AbS at the M06-2X/def2-TZVP level are shown in Figure 6. For the isomerization of single-molecule *p*-AbS and *m*-AbS, the pathway through TS1 was also advantageous. The energy barrier of TS1 was lower by 5.1 kcal/mol than TS2. This may be due to the smaller steric hindrance when passing through the vibration mode of TS1, so isomerism was more likely to occur. The optimized structures for AbS along the isomerization pathway are shown in Figure 7. It can be seen that in the isomerization process of AbS, the change of AbS structure was almost the same as that of AbS$^-$ in the composites. The isomerization processes of *p*-CAbS and *m*-CAbS were also one-step concerted processes with the inversion of C(2)N(3)N(4) and the rotation of the unsubstituted benzene ring around the C(2)-N(3) bond.

By comparing the free energy profiles of the isomerization pathways of AbS$^-$-LDHs and AbSs, it was obvious that the LDH host molecule affected the isomerization for AbS$^-$ guest

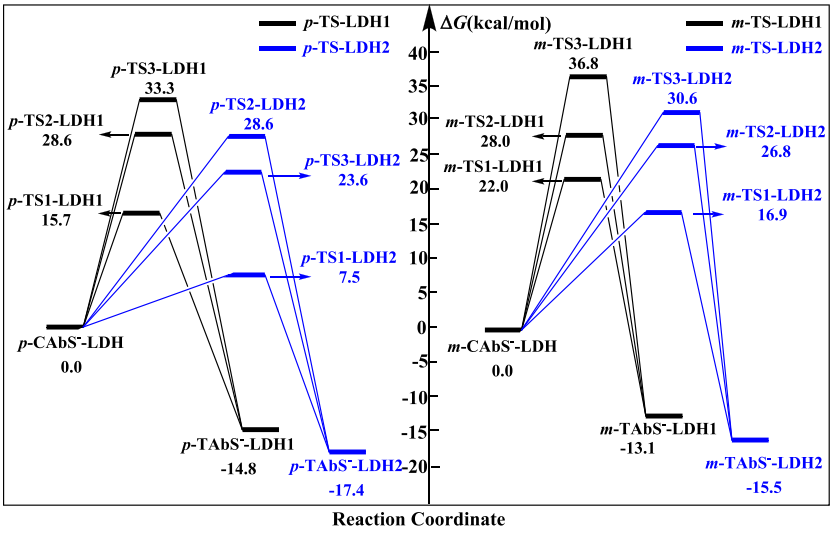

Figure 5. Free energy profiles of the isomerization for *p*- and *m*-CAbS$^-$-LDH at the M06-2X/def2-TZVP//M06-2X/6-31G(d,p) level.

https://doi.org/10.1021/acsomega.3c00791
ACS Omega 2023, 8, 11596−11606

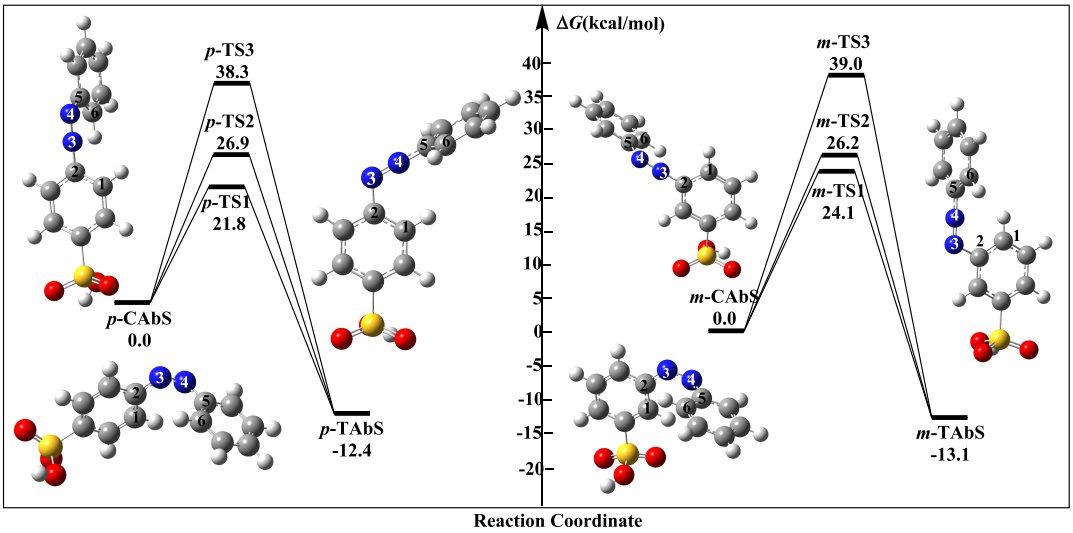

Figure 6. Free energy profiles of isomerization for *p*-CAbS and *m*-CAbS at the M06-2X/def2-TZVP//M06-2X/6-31G(d,p) level.

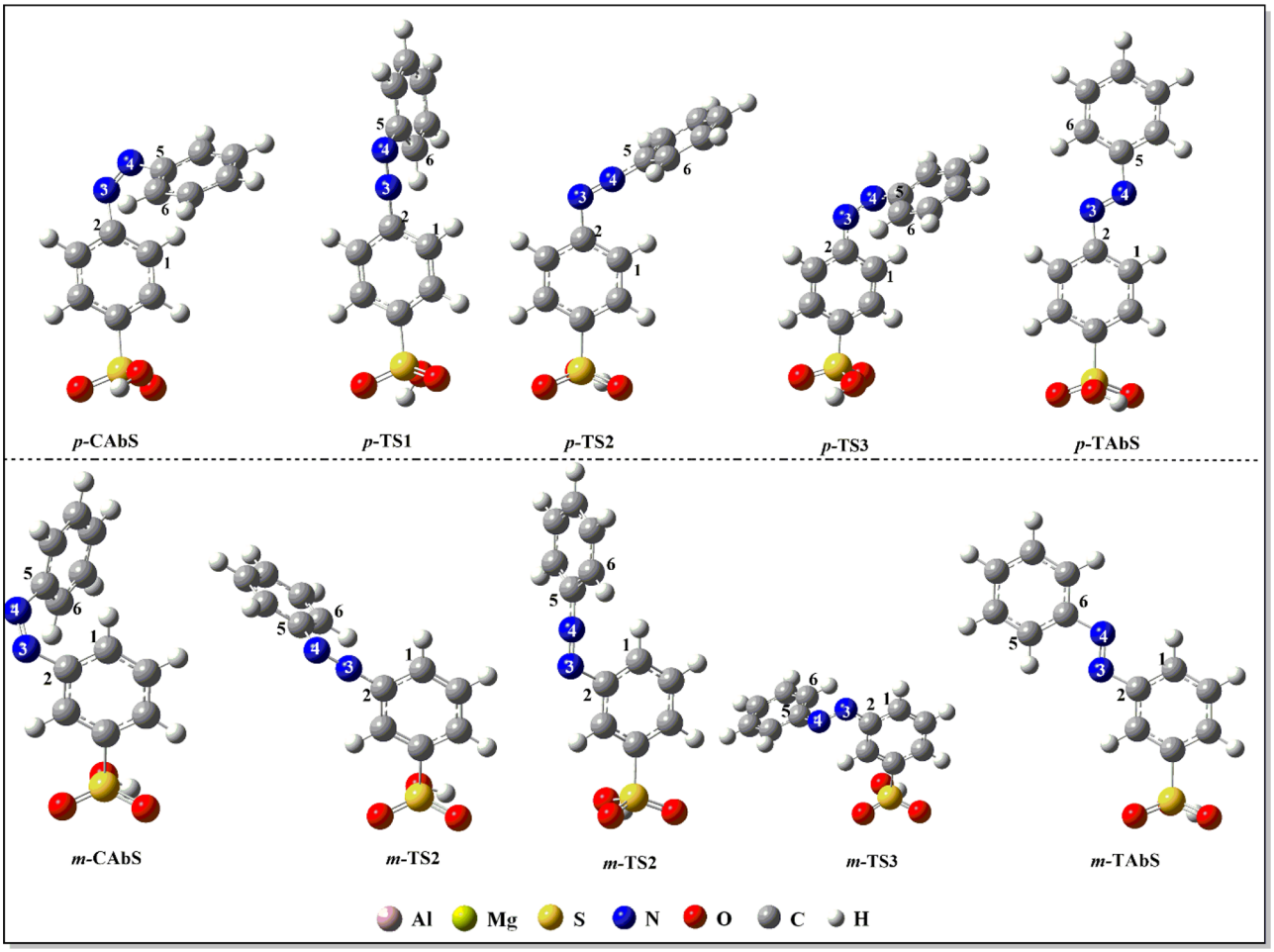

Figure 7. Optimized stable structures along the isomerization pathway of *p*-AbS and *m*-AbS at the M06-2X/6-31G(d,p) level.

anions. The addition of LDH lamella could lower the isomerization energy barrier of $CAbS^-$ anions. It was worth noting that the physicochemical properties of LDH could be tuned through the assembly of AbS^- anions into LDH layers, which provide insights into the development of new functional intercalation materials.

3.3. Spectroscopic Properties of AbS^--LDH.

trans-Azobenzene could be easily converted into a *cis* structure under visible light irradiation. The TD-DFT method could be used to calculate reliable low-excited state properties, but the results of higher excited states have larger errors. Therefore, the first 50 singlet excited states of each isomer are calculated.[46] The properties of singlet vertical excited states

https://doi.org/10.1021/acsomega.3c00791
ACS Omega 2023, 8, 11596−11606

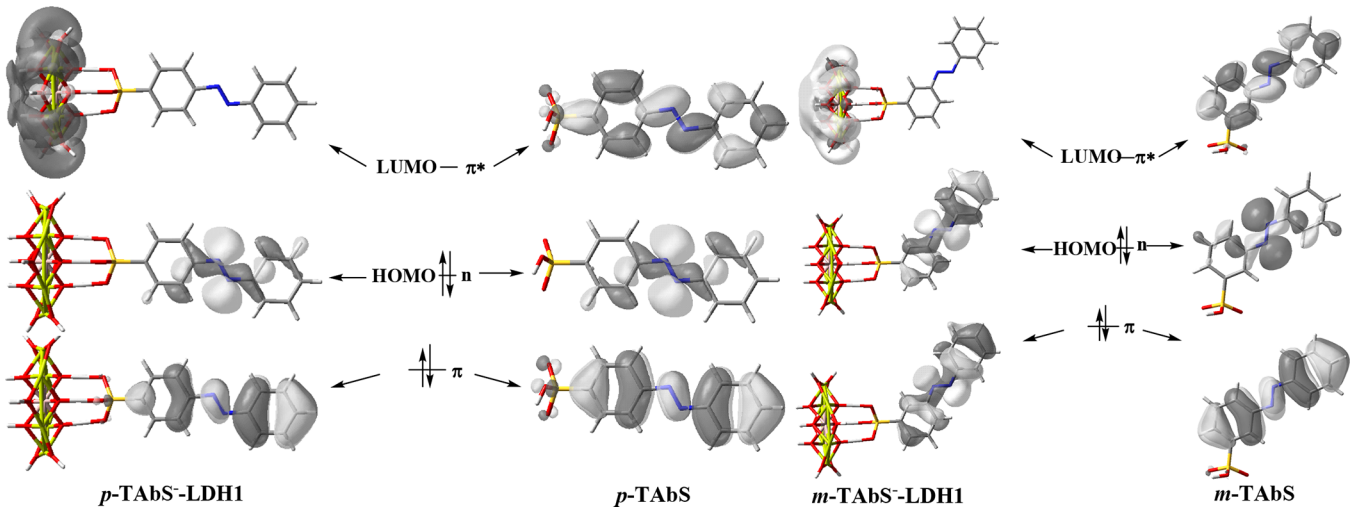

Figure 8. Frontier molecular orbitals of TAbS$^-$-LDH1 and TAbS at the M06-2X/6-31G(d,p) level.

for single-molecule *p*-TAbS, *m*-TAbS, supramolecules *p*-TAbS$^-$-LDH1, *m*-TAbS$^-$-LDH1, *p*-TAbS$^-$-LDH2, and *m*-TAbS$^-$-LDH2 were calculated at the M06-2X/6-31G(d,p) level. The calculated frontier molecular orbitals indicated that the HOMO-1 orbital was the π orbital on the benzene ring, the HOMO orbital was the n orbital formed by the lone pair of electrons on the N atoms, and the LUMO orbital was the π^* orbital on the benzene ring. The HOMO → LUMO corresponds to n → π^* transition, and HOMO-1 → LUMO corresponds to π → π^* transition. The n → π^* transitions were due to a lone pair of electrons on the central N atoms, and the π → π^* transitions were delocalized in the two benzene rings (see Figure 8). The electronic excitation energies of these transitions are listed in Table 3.

Table 3. Electronic Absorption Spectra of *cis* and *trans*-Isomers for AbS and AbS$^-$-LDH at the M06-2X/6-31G(d,p) Level.

	$S_1 \leftarrow S_0(n \rightarrow \pi^*)$		$S_2 \leftarrow S_0(\pi \rightarrow \pi^*)$		
	E_{ex}/eV	λ/nm	E_{ex}/eV	λ/nm	energy difference/eV (E_{ex} ($S_2 \leftarrow S_0$) − E_{ex} ($S_1 \leftarrow S_0$))
p-CAbS$^-$-LDH1	2.44	508	3.77	329	1.33
p-TAbS$^-$-LDH1	2.40	517	3.94	315	1.54
p-CAbS$^-$-LDH2	2.35	528	2.80	443	0.45
p-TAbS$^-$-LDH2	2.28	545	2.68	462	0.40
p-CAbS	2.34	529	4.66	266	2.32
p-TAbS	2.46	504	4.21	295	1.75
m-CAbS$^-$-LDH1	2.45	506	3.72	333	1.27
m-TAbS$^-$-LDH1	2.49	498	3.95	314	1.46
m-CAbS$^-$-LDH2	2.35	528	2.72	455	0.37
m-TAbS$^-$-LDH2	2.46	505	2.79	445	0.39
m-CAbS	2.44	508	4.69	264	2.25
m-TAbS	2.44	508	4.15	299	1.71

The transition energy ($E_{ex}(S_1 \leftarrow S_0)$) for *p*-TAbS was 2.46 eV, which correspond to the maximum of the $S_1 \leftarrow S_0$ absorption wavelength at 504 nm. The transition energy of $S_2 \leftarrow S_0$ was 4.21 eV, and the corresponding absorption wavelength was 295 nm. For the *p*-TAbS$^-$-LDH1 supramolecule, the transition energy of $S_1 \leftarrow S_0$ was 2.40 eV, and its maximum absorption wavelength showed a 13 nm red-shift compared with that of the *p*-TAbS molecule. The transition energy of $S_2 \leftarrow S_0$ was 3.94 eV, and its maximum absorption wavelength showed a 20 nm red-shift. However, the energy gap of $S_1 \leftarrow S_0$ transition for *m*-TAbS$^-$-LDH1 was larger than that of the *m*-TAbS molecule, corresponding to the maximum absorption wavelength with a blue-shift of 10 nm, while the energy gap of $S_2 \leftarrow S_0$ transition for *m*-TAbS$^-$-LDH1 was smaller than that of *m*-TAbS, corresponding to the maximum absorption wavelength with a red-shift of 15 nm. When the Mg-Al-LDH lamella and AbS$^-$ were combined by hydrogen bond interaction, if the energy of the n or π orbital decreased, a blue-shift would occur; otherwise, a red-shift would occur.

The excitation of the *cis*-isomer of *p*-AbS$^-$-LDH1 and *p*-AbS was different from those of corresponding *trans*-isomers, and the $S_1 \leftarrow S_0$ transition of the *cis*-isomer was slightly intensive due to its twisted configuration, while the intensities of $S_2 \leftarrow S_0$ transitions for *cis*-isomers were low. When *p*-TAbS$^-$-LDH1 and *p*-TAbS were converted into *p*-CAbS$^-$-LDH1 and *p*-CAbS, respectively, the n → π^* transitions were changed from a forbidden state to an allowable state due to the transformation from the planar configuration to the non-planar one. *m*-TAbS, *m*-TAbS$^-$-LDH1, and *m*-TAbS$^-$-LDH2 showed similar spectroscopic properties compared with para-substituted ones. Also, the spectral properties of AbS$^-$ molecules with LDH2 were similar to those with LDH1. The maximum absorption wavelength of $S_1 \leftarrow S_0$ and $S_2 \leftarrow S_0$ of *p*-TAbS$^-$-LDH2 showed a red-shift compared with that of the *p*-TAbS molecule; $S_1 \leftarrow S_0$ and $S_2 \leftarrow S_0$ of *m*-TAbS$^-$-LDH2 showed a blue-shift and a red-shift compared with those of the *m*-TAbS molecule, respectively. When *p*-TAbS$^-$-LDH2 was converted into *p*-CAbS$^-$-LDH2, the n → π^* transitions were changed from a forbidden state to an allowable state.

The frontier molecular orbital energy gaps ($\Delta\varepsilon$) could reflect the transition ability of electrons from occupied molecular orbitals to unoccupied molecular orbitals, and it could show the difficulty of a molecule to be excited. It could be seen that the LDH lamella could reduce the energy gap of the n → π^* and π → π^* electronic transition and lead to a red-shift in the absorption spectra (see Table 4).

The UV spectrum shows that azobenzene sulfonic acid was mainly concentrated in the K band around the period of 125−225 nm and the R band around the period of 225−400 nm in the UV−visible absorption region (see Figure 9). When the

https://doi.org/10.1021/acsomega.3c00791
ACS Omega 2023, 8, 11596−11606

Table 4. ε_{HOMO} and ε_{LUMO} and Energy Gaps ($\Delta\varepsilon$) of AbS$^-$-LDH and AbS at the M06-2X/6-31G(d,p) Level (Unit: eV)

	ε_{HOMO-1}	ε_{HOMO}	ε_{LUMO}	$\Delta\varepsilon_1{}^a$	$\Delta\varepsilon_2{}^b$
p-CAbS$^-$-LDH1	−11.5	−10.6	−5.6	5.1	5.9
p-TAbS$^-$-LDH1	−11.1	−10.7	−6.1	4.7	5.0
p-CAbS$^-$-LDH2	−14.2	−13.6	−10.2	3.4	4.1
p-TAbS$^-$-LDH2	−13.7	−13.4	−10.1	3.3	3.6
p-CAbS	−8.8	−7.7	−0.3	7.5	8.5
p-TAbS	−8.5	−8.0	−0.2	7.9	8.3
m-CAbS$^-$-LDH1	−11.4	−10.6	−6.1	4.5	5.3
m-TAbS$^-$-LDH1	−11.2	−10.7	−6.1	4.6	5.1
m-CAbS$^-$-LDH2	−14.2	−13.6	−10.2	3.4	4.1
m-TAbS$^-$-LDH2	−13.9	−13.6	−10.1	3.5	3.8
m-CAbS	−8.7	−7.7	−1.3	6.4	7.4
m-TAbS	−8.4	−7.9	−1.8	3.9	6.2

$^a\Delta\varepsilon_1 = \varepsilon_{LUMO} - \varepsilon_{HOMO}$ $^b\Delta\varepsilon_2 = \varepsilon_{LUMO} - \varepsilon_{HOMO-1}$.

AbS$^-$ combined with LDHs, a significant red-shift was observed, which was consistent with the result of the frontier molecular orbital energy gaps, and the K band changed from 125−220 nm to 175−250 nm. This may be in that the hydrogen bond formed by the hydrogen atom of the hydroxyl group of the LDH and the oxygen atom of the sulfonate enhanced the degree of conjugation. As a result, the energy gap was reduced, leading to the red-shift, and the absorption spectrum was broadened. However, for the CAbS$^-$-LDH1 structure, only the K band had a red-shift about 50 nm, while the R band changed insignificantly, which may be due to the saddle shape of the *cis*-structure causing the overall structure to be non-planar, and the degree of planar conjugation was weakened.

The absorption wavelength of solute can also be shifted due to the influence of the formation of hydrogen bonds between the solvent and the solute molecules and the dipolar polarization. Therefore, the influence of solvents on spectral properties was also studied. As shown in Figure 10a, for the n → π^* transition, in the polar solvent DMSO, the n orbital energy of the ground state molecules was reduced, and the energy absorbed during the n → π^* transition was larger, which made the absorption shift to the short-wave direction and caused a blue-shift phenomenon (see Table S1). In the non-polar solvent CCl_4, the energy of the n → π^* transition was also increased, which changed a little compared to that in DMSO solvent. This implied that polar solvents had a greater influence on the absorption wavelength than non-polar solvents. For the π → π^* transition, the energy difference between the ground state and the excited state was reduced for

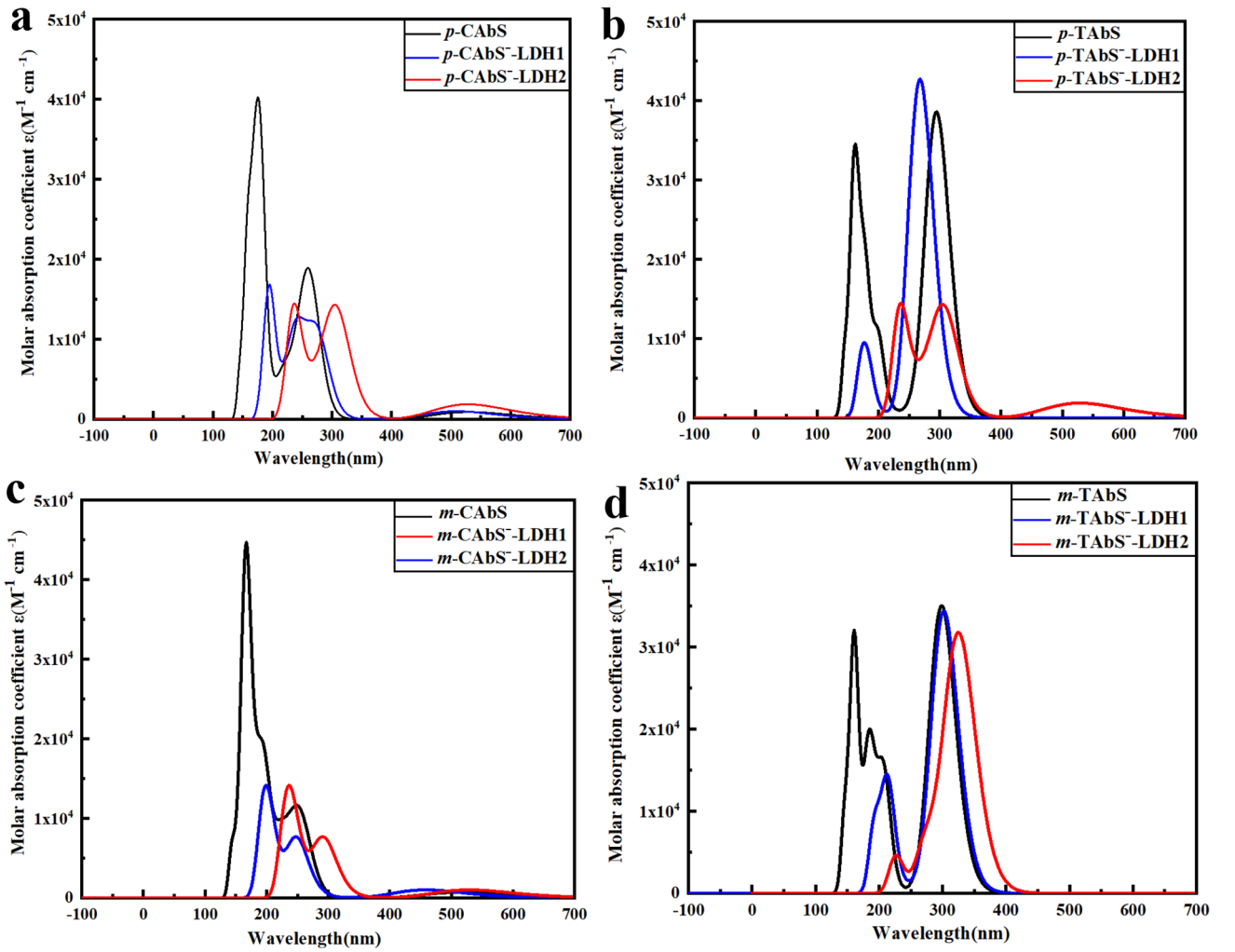

Figure 9. Absorption spectra of (a) *p*-CAbS and *p*-CAbS$^-$-LDHs; (b) *p*-TAbS and *p*-TAbS$^-$-LDHs; (c) *m*-CAbS and *m*-CAbS$^-$-LDHs; and (d) *m*-TAbS and *m*-TAbS$^-$-LDHs.

https://doi.org/10.1021/acsomega.3c00791
ACS Omega 2023, 8, 11596−11606

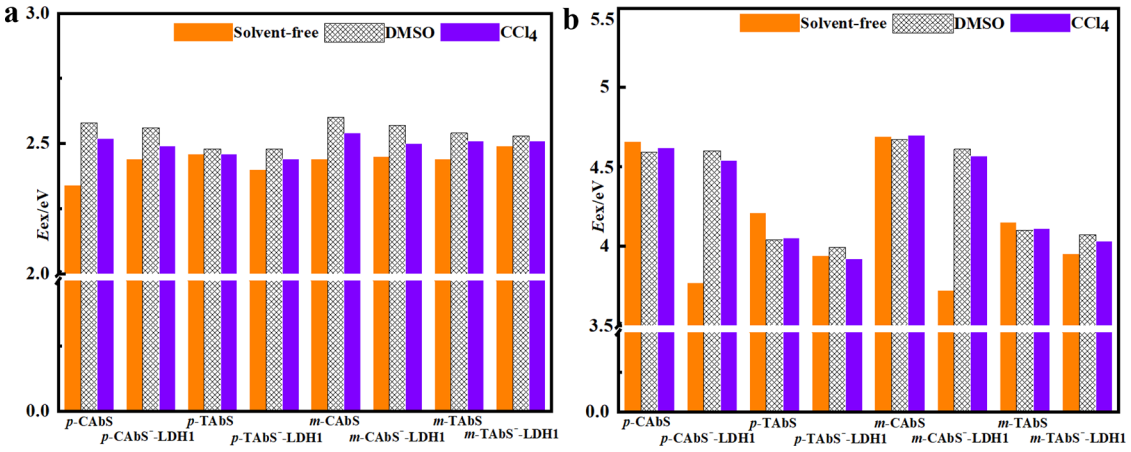

Figure 10. (a) Influence of solvent on the energy of n → π^* transition. (b) Influence of solvent on the energy of $\pi \rightarrow \pi^*$ transition (Ordinate E_{ex} refers to the transition energy).

AbS in the polar solvent DMSO, and the absorption was shifted to the long-wave region, that is, the red-shift phenomenon occurred. As for the composite AbS$^-$-LDH1, the energy absorbed during the $\pi \rightarrow \pi^*$ transition was larger, causing the absorption shift to the short-wave direction (see Figure 10b). Similarly, when in the polar solvent DMSO and the non-polar solvent CCl_4, energy gaps ($\Delta\varepsilon$) of AbS$^-$-LDH1 and AbS showed the same pattern (see Table S2).

4. CONCLUSIONS

The photothermal properties of supramolecular structures of AbS$^-$-LDHs were studied at the M06-2X/def2-TZVP//M06-2X/6-31G(d,p) level as well as those of single AbS molecules. The calculated results showed that the hydrogen bond interaction between AbS$^-$ and LDH1 was stronger and the structure was more stable. The addition of LDH lamella could lower the isomerization energy barrier of CAbS$^-$ anions compared to the single molecule. The LDH lamella made the AbS spectrum red-shift, and the optical properties were better in the polar solvent DMSO than in the non-polar solvent CCl_4. For the isomerization reaction of AbS$^-$-LDH and AbS, the pathway through the transition state TS1 was favorable. The energy barrier of *p*-TS1-LDH1 was lower by 12.9 kcal/mol than *p*-TS2-LDH1, and the energy barrier of *p*-TS1-LDH2 was lower by 16.1 kcal/mol than *p*-TS3-LDH2. The energy barrier of *p*-TS1 was lower by 5.1 kcal/mol than *p*-TS2. Meanwhile, on their spectroscopic properties, the $S_1 \leftarrow S_0$ and $S_2 \leftarrow S_0$ transitions for both TAbS$^-$-LDHs and TAbS molecules appeared exceedingly similar: the $S_1 \leftarrow S_0$ transition was forbidden, and the $S_2 \leftarrow S_0$ transition was allowed. It was found that there is a red-shift in $S_1 \leftarrow S_0$ and $S_2 \leftarrow S_0$ transition, and energy gaps were decreased with the addition of LDH lamella. In summary, AbS$^-$-LDHs are potential composite materials owning better stability than single AbSs.

■ ASSOCIATED CONTENT

Supporting Information

The Supporting Information is available free of charge at https://pubs.acs.org/doi/10.1021/acsomega.3c00791.

Relevant reaction mechanism, analysis results, and the geometric coordinates of the main structures (optimized structures, key structural parameters, electronic absorption spectra, ε_{HOMO}, ε_{LUMO}, and energy gaps, free energy profiles, and Cartesian coordinates) (PDF)

■ AUTHOR INFORMATION

Corresponding Authors

Ming Lei − *State Key Laboratory of Chemical Resource Engineering, College of Chemistry, Institute of Computational Chemistry, Beijing University of Chemical Technology, Beijing 100029, P. R. China*; orcid.org/0000-0001-5765-9664; Email: leim@mail.buct.edu.cn

Min Pu − *State Key Laboratory of Chemical Resource Engineering, College of Chemistry, Institute of Computational Chemistry, Beijing University of Chemical Technology, Beijing 100029, P. R. China*; orcid.org/0000-0001-5212-728X; Email: pumin@mail.buct.edu.cn

Authors

Peihuan Zhang − *State Key Laboratory of Chemical Resource Engineering, College of Chemistry, Institute of Computational Chemistry, Beijing University of Chemical Technology, Beijing 100029, P. R. China*

Yue Zhu − *State Key Laboratory of Chemical Resource Engineering, College of Chemistry, Institute of Computational Chemistry, Beijing University of Chemical Technology, Beijing 100029, P. R. China*

Zhewei Li − *State Key Laboratory of Chemical Resource Engineering, College of Chemistry, Institute of Computational Chemistry, Beijing University of Chemical Technology, Beijing 100029, P. R. China*

Luocong Wang − *State Key Laboratory of Chemical Resource Engineering, College of Chemistry, Institute of Computational Chemistry, Beijing University of Chemical Technology, Beijing 100029, P. R. China*

Caiwei Yue − *State Key Laboratory of Chemical Resource Engineering, College of Chemistry, Institute of Computational Chemistry, Beijing University of Chemical Technology, Beijing 100029, P. R. China*

Complete contact information is available at: https://pubs.acs.org/10.1021/acsomega.3c00791

Author Contributions

The manuscript was written through contributions of all authors. All authors have given approval to the final version of the manuscript.

Notes

The authors declare no competing financial interest.

https://doi.org/10.1021/acsomega.3c00791
ACS Omega 2023, 8, 11596−11606

■ ACKNOWLEDGMENTS

This work is supported by the National Natural Science Foundation of China (Grant No. 22073005). We also thank the High Performance Computing (HPC) Platform at Beijing University of Chemical Technology (BUCT) for providing part of the computational resources.

■ REFERENCES

(1) Crespi, S.; Simeth, N. A.; König, B. Heteroaryl Azo Dyes as Molecular Photoswitches. *Nat. Rev. Chem.* **2019**, *3*, 133−146.
(2) Zarins, E.; Balodis, K.; Ruduss, A.; Kokars, V.; Ozols, A.; Augustovs, P.; Saharovs, D. Molecular Glasses of Azobenzene for Holographic Data Storage Applications. *Opt. Mater.* , *79*, 45−52, DOI: 10.1016/j.optmat.2018.03.020.
(3) Yamada, S.; Bessho, J.; Nakasato, H.; Tsutsumi, O. Color Tuning Donor−Acceptor-Type Azobenzene Dyes by Controlling the Molecular Geometry of the Donor Moiety. *Dyes Pigm.* **2017**, *150*, 89−96.
(4) Goda, K.; Omori, M.; Takatoh, K. Optical Switching in Guest-Host Liquid Crystal Devices Driven by Photo- And Thermal Isomerisation of Azobenzene. *Liq. Cryst.* **2018**, *45*, 489−450.
(5) Delaire, J. A.; Nakatani, K. Linear and Nonlinear Optical Properties of Photochromic Molecules and Materials. *Chem. Rev.* **2000**, *100*, 1817−1846.
(6) Natansohn, A.; Rochon, P. Photoinduced Motions in Azo-Containing Polymers. *Chem Rev.* **2003**, *34*, 4139−4175.
(7) Berg, R. H.; Ramanujam, P. S.; Hvilsted, S. Peptide Oligomers for Holographic Data Storage. *Nature* **1996**, *383*, 505−508.
(8) Muraoka, T.; Kinbara, K.; Kobayashi, Y.; Aida, T. Light-Driven Open-Close Motion of Chiral Molecular Scissors. *J. Am. Chem. Soc.* **2003**, *125*, 5612.
(9) Hashidzume, A.; Yamaguchi, H.; Harada, A. Cyclodextrin-Based Molecular Machines. *Top. Curr. Chem.* **2014**, *354*, 71−110.
(10) Balzani, V.; Credi, A.; Marchioni, F.; Stoddart, J. F. Artificial Molecular-Level Machines. Dethreading−Rethreading of a Pseudorotaxane Powered Exclusively by Light Energy. *Chem. Commun.* **2001**, *18*, 1860−1861.
(11) Banerjee, I. A.; Yu, L.; Matsui, H. Application of Host-Guest Chemistry in Nanotube-Based Device Fabrication: Photochemically Controlled Immobilization of Azobenzene Nanotubes on Patterned Alpha-Cd Monolayer/Au Substrates via Molecular Recognition. *J. Am. Chem. Soc.* **2003**, *125*, 9542−9543.
(12) Schlachter, A.; Asselin, P.; Harvey, P. D. Porphyrin-Containing MOFs and COFs as Heterogeneous Photosensitizers for Singlet Oxygen-Based Antimicrobial Nanodevices. *ACS Appl. Mater. Interfaces* **2021**, *13*, 26651−26672.
(13) Blevins, A. A.; Blanchard, G. J. Effect of Positional Substitution on the Optical Response of Symmetrically Disubstituted Azobenzene Derivatives. *J. Phys. Chem. B* **2004**, *108*, 4962−4968.
(14) Miniewicz, A.; Orlikowska, H.; Sobolewska, A.; Bartkiewicz, S. Kinetics of Thermal Cis−Trans Isomerization in a Phototropic Azobenzene-Based Single-Component Liquid Crystal in Its Nematic And Isotropic Phases. *Phys. Chem. Chem. Phys.* **2018**, *20*, 2904−2913.
(15) CreCcA, C. R.; Roitberg, A. E. Theoretical Study of the Isomerization Mechanism of Azobenzene and Disubstituted Azobenzene Derivatives. *J. Phys. Chem. A* **2006**, *110*, 8188−8203.
(16) Zhou, W.; Grosjean, S.; BrSe, S.; Heinke, L. Thermal cis-to-trans Isomerization of Azobenzene Side Groups in Metal-Organic Frameworks investigated by Localized Surface Plasmon Resonance Spectroscopy. *Z. Phys. Chem.* **2019**, *233*, 15−22.
(17) Smith, S.; Abdallah, F. B. The Kinetics of the Cis-to-Trans Thermal Isomerization of 4-Anilino-4′- Nitroazobenzene are Highly Influenced by Solvent Polarity. *J. Thermodyn. Catal.* **2017**, *8*, 181−186.
(18) Takei, M.; Yui, H.; Hirose, Y.; Sawada, T. Femtosecond Time-Resolved Spectroscopy of Photoisomerization of Methyl Orange in Cyclodextrins. *J. Phys. Chem. A* **2001**, *105*, 11395−11399.
(19) Kojima, M.; Nakajoh, M.; Nebashi, S.; Kurita, N. Effect of metal cation on photoisomerization of azobenzenes in zeolite nanocavities. *Res. Chem. Intermed.* **2004**, *30*, 181−190.
(20) Zhu, M. X.; Li, Y. P.; Xie, M.; Xin, H. Z. Sorption of an Anionic Dye by Uncalcined and Calcined Layered Double Hydroxides: A Case Study. *J. Hazard. Mater.* **2005**, *120*, 163−171.
(21) Padula, I. D.; Santos, B.; Rodrigues, A.; Gastelois, P. L.; Oliveira, C. C. Niobium-Modified Hydrotalcite Catalysts: Sustainable Conversion of Waste Glycerol to Valuable Chemicals. *Appl. Catal., A* **2020**, *606*, 117814−117823.
(22) Yan, J.; Chen, Y.; Gao, W.; Yun, L.; Lu, Q. Catalysis of Hydrogen Peroxide with Cu Layered Double Hydrotalcite for the Degradation of Ethylbenzene. *Chemosphere* **2019**, *225*, 157−165.
(23) Hao, J. J.; Miao, H. J.; Medicine, D. O. Clinical Study on Weiyankang Capsules Combined with Hydrotalcite in Treatment of Bile Reflux Gastritis. *Drug. Clin* **2016**, *31*, 1542.
(24) Maretti, L.; Carbonell, E.; Alvaro, M.; Scaiano, J. C.; Garcia, H. Laser Flash Photolysis of Dioxo Iron Phthalocyanine Intercalated in Hydrotalcite and Its Use As a Photocatalyst. *J. Photoch. Photobio. A* **2009**, *205*, 19−22.
(25) Zhao, Y.; Zhang, S.; Bei, L.; Yan, H.; Shan, H.; Lei, T.; Shi, W.; Ma, J.; Wei, M.; Evans, D. G. A Family of Visible-Light Responsive Photocatalysts Obtained by Dispersing CrO6 Octahedra Into a Hydrotalcite Matrix. *Chem. − Eur. J.* **2011**, *17*, 13175−13181.
(26) Wang, C.; Pu, M.; Zhang, P.; Gao, Y.; Yang, Z.; Lei, M. Structure Simulation and Host−Guest Interaction of Histidine-Intercalated Hydrotalcite−Montmorillonite Complex. *Minerals* **2018**, *8*, 198.
(27) Yano, A.; Konno, Y.; Kinoshita, E.; Yano, R. Concentration Dependence of Thermal Isomerization Process of Methyl Orange in Ethanol. *J. Photoch. Photobio. A* **2017**, *346*, 411−415.
(28) Liu, Y.; Gao, Y.; Zhang, Z.; Wang, Q. Preparation of Ammonium Polyphosphate and Dye Co-Intercalated LDH/Polypropylene Composites with Enhanced Flame Retardant and UV Resistance Properties. *Chemosphere* **2021**, *277*, 130370−130378.
(29) Naseem, S.; Gevers, B. R.; Labuschagne, J.; Leuteritz, A. Preparation of Photoactive Transition-Metal Layered Double Hydroxides (LDH) to Replace Dye-Sensitized Materials in Solar Cells. *Materials* **2020**, *13*, 4384.
(30) Liu, L. Y.; Min, P.; Lan, Y.; Li, D. Q.; Evans, D. G.; He, J. Experimental and Theoretical Study on The Structure of Acid Orange 7-Pillared Layered Double Hydroxide. *Mater. Chem. Phys.* **2007**, *106*, 422−427.
(31) Taviot-Gueho, C.; Illaik, A.; Vuillermoz, C.; Commereuc, S.; Verney, V.; Leroux, F. LDH−dye Hybrid Material as Coloured Filler into Polystyrene: Structural Characterization and Rheological Properties. *J. Phys. Chem. Solids* **2007**, *68*, 1140−1146.
(32) Melánová, K.; Bene, L.; Zima, V.; Svoboda, J. Intercalation of Dyes Containing SO_3H Groups into Zn−Al Layered Double Hydroxide. *J. Incl. Phenom. Macro.* **2005**, *51*, 97−101.
(33) Hussein, M.; Zainal, Z.; Yahaya, A. H.; Aziz, A. Synthesis of Layered Organic−Inorganic Nanohybrid Material: An Organic Dye, Naphthol Blue Black in Magnesium−Aluminum Layered Double Hydroxide Inorganic Lamella. *Mater. Sci. Eng., B* **2002**, *88*, 98−102.
(34) Hussein, M.; Yahaya, A. H.; Shamsul, M.; Salleh, H. M.; Yap, T.; Kiu, J. Acid Fuchsin-Interleaved Mg−Al-Layered Double Hydroxide for The Formation of an Organic−Inorganic Hybrid Nanocomposite. *Mater. Lett.* **2004**, *58*, 329−332.
(35) Yuan, Y. X.; Wang, L.; Han, Y. F.; Li, F. F.; Wang, H. B. A Novel Azo-Thiourea Based Visible Light Switchable Anion Receptor. *Tetrahedron Lett.* **2016**, *57*, 878−882.
(36) Laguna, H.; Loera, S.; Ibarra, I. A.; Lima, E.; Lara, V. Azoic Dyes Hosted on Hydrotalcite-Like Compounds: Non-Toxic Hybrid Pigments. *Micropor. Mesopor. Mater.* **2012**, *98*, 234−241.
(37) Hussein, M. Z. B.; Yahaya, A. H.; Ping, L. M. Dye-Interleaved Nanocomposite: Evan's Blue in the Lamella of Mg−Al-Layered Double Hydroxide. *Mater. Lett.* **2004**, *63*, 135−140.
(38) Zhu, Y.; Pu, M.; Fang, D. C.; He, J.; Evans, D. G. A Density Functional Theory Study on the Thermal and Photochemical

https://doi.org/10.1021/acsomega.3c00791
ACS Omega 2023, 8, 11596−11606

Isomerization Mechanism of 4,4′-Azobenzene Disulfonate. *J. Photoch. Photobio. A* **2010**, *211*, 89−98.
(39) Pu, M.; Zhang, B. F. Theoretical Study on the Microstructures of Hydrotalcite Lamellae with Mg/Al Ratio of Two. *Mater. Lett.* **2005**, *59*, 3343−3347.
(40) Pu, M.; Wang, Y. L.; Liu, L. Y.; Liu, Y. H.; He, J.; Evans, D. G. Quantum Chemistry and Molecular Mechanics Studies of the Lamella Structure of Hydrotalcite with Mg/Al Ratio Of 3. *J. Phys. Chem. Solids* **2008**, *69*, 1066−1069.
(41) Zhao, Y.; Truhlar, D. G. A New Local Density Functional for Main-Group Thermochemistry, Transition Metal Bonding, Thermochemical Kinetics, and Noncovalent Interactions. *J. Chem. Phys.* **2006**, *125*, 194101−194118.
(42) Rodrigues, G. L.; Rocha, W. R. Formation and Release of NO from Ruthenium Nitrosyl Ammine Complexes $[Ru(NH_3)_5(NO)]^{(2+/3+)}$ in Aqueous Solution: A Theoretical Investigation. *J. Phys. Chem. B* **2016**, *120*, 11821−11833.
(43) Keisuke, K.; Yuki, N.; Taro, S. Time-Resolved High-Harmonic Spectroscopy of Ultrafast Photoisomerization Dynamics. *Opt. Express* **2018**, *26*, 31039−31054.
(44) Shivade, R. K.; Chakraborty, B. Optical Absorption Spectra of Boron Clusters Bn (N = 2−5) for Application in Nano Scintillator − A Time Dependent Density Functional Theory Study. *Eur. Phys. J. B* **2016**, *89*, 198−211.
(45) Jfg, M.; Trucks, W.; Schlegel, H. B.; Scuseria, G. E.; Robb, M. A.; Cheeseman, J. R.; Scalmani, G.; Barone, V.; Mennucci, B.; Petersson, G. A., *Gaussian 09*, Revision A. 1; Gaussian. 2009.
(46) Chi, S. M.; Li, L.; Chen, Y.; Fu, W. F. Molecular Geometries and Theoretical Electronic Spectra of Four 1,8-Naphthyridine Derivatives. *Spectrosc. Spectral Anal.* **2010**, *30*, 586.

https://doi.org/10.1021/acsomega.3c00791
ACS Omega 2023, 8, 11596−11606